Good Solvent Effects of C_{70} Cluster Formations and Their Electron-Transporting and Photoelectrochemical Properties†

Noriyasu Tezuka,‡ Tomokazu Umeyama,‡ Yoshihiro Matano,‡ Tetsuya Shishido,‡ Mitsuo Kawasaki,‡ Masayuki Nishi,§ Kazuyuki Hirao,§ Heli Lehtivuori,|| Nikolai V. Tkachenko,|| Helge Lemmetyinen,|| Yoshihito Honsho,⊥ Shu Seki,*,⊥,# and Hiroshi Imahori*,‡,∇,◆

Department of Molecular Engineering, Graduate School of Engineering, Department of Material Chemistry, Graduate School of Engineering, and Institute for Integrated Cell-Material Sciences (iCeMS), Kyoto University, Nishikyo-ku, Kyoto 615-8510, Japan, Department of Chemistry and Bioengineering, Tampere University of Technology, P.O. Box 541, FIN-33101 Tampere, Finland, Department of Applied Chemistry, Graduate School of Engineering, Osaka University, 2-1, Yamadaoka, Suita, Osaka 565-0871, Japan, PRESTO, Japan Science and Technology Agency, 4-1-8 Honcho, Kawaguchi, Saitama 332-0012, Japan, and Fukui Institute for Fundamental Chemistry, Kyoto University, 34-4, Takano-Nishihiraki-cho, Sakyo-ku, Kyoto 606-8103, Japan

Received: November 23, 2009; Revised Manuscript Received: January 5, 2010

Good solvent effects of C_{70} cluster formations and their electron-transporting and photoelectrochemical properties have been systematically examined for the first time. Nano-to-micrometer scale assemblies of C_{70} with different morphologies were prepared by rapidly injecting poor solvent (i.e., acetonitrile) into a solution of C_{70} dissolved in various good solvents (i.e., benzene, toluene, chlorobenzene, etc). The cluster morphology engineering was successfully achieved by changing the good solvent, yielding the spherical, rodlike, or platelike clusters in the mixed solvents. The clusters of C_{70} were electrophoretically deposited onto a nanostructured SnO_2 electrode to examine the photoelectrochemical properties under the white light or monochromatic light illumination. The maximum incident photon-to-current efficiency (IPCE) varied from 0.8 to 10% depending on the combinations of the poor-good solvents. The differences in the IPCE values are discussed in terms of the surface area, thickness, and electron mobility of the deposited cluster films. The electron mobility is found to be the most predominant factor for the IPCE, indicating the importance of the electron-transporting process in the overall photocurrent generation. In addition, the electron mobility is closely correlated with the underlying molecular alignment and the resultant cluster structure. Thus, these results will provide basic clue for the design of C_{70}-based molecular devices including the organic photovoltaics.

Introduction

Self-assembled molecular architectures have attracted considerable attention due to their promising application toward bottom-up approaches to nanotechnology.[1] In particular, shape-defined assemblies with nano-to-micrometer dimensions can be potentially harnessed as building blocks of next-generation optoelectronic devices.[1,2] One of the key components to construct such molecular nanostructures is fullerenes and their derivatives. So far, the preparation of fullerene-based assemblies like nanorod,[3,4] nanofiber (or nanowhisker),[5,6] nanotube,[7] nanosheet,[8] nanoflower,[9] nanoparticle,[10] and others[11] have been reported, all of which deserve special interests from a perspective of material research because of their unique morphologies. On the other hand, those nanostructures of fullerenes provoke another interest relating to the state-of-the-art bulk heterojunction (BHJ) solar cells, where the morphological control of fullerene nanodomains in the blend film with conjugated polymers is essential to achieve high cell performance.[12,13] Indeed, elucidation of the photoelectrochemical properties of fullerene-based nanostructures would offer fundamental information toward designing highly efficient BHJ devices. However, there are limited number of studies focusing on the photoelectrochemical properties of nanostructured fullerene assemblies.[11d,14,15] As such, systematic comparison of the photoelectrochemical properties of fullerene-based assemblies and/or their composite films with different nano-to-micrometer scale morphologies has yet to be conducted.

One of the most frequently employed approaches to prepare fullerene assemblies is rapid injection technique first demonstrated by Sun and Bunker, where a poor solvent (e.g., acetonitrile) is rapidly injected into a solution of fullerene dissolved in good solvent (e.g., benzene, toluene, etc.) or vice versa.[15–19] The lyophobic interaction between the mixed solvent and fullerene molecules as well as the $\pi-\pi$ interaction between fullerene molecules is responsible for formation of the metastable colloidal aggregates in the mixed solvent. Most prominent advantage of the rapid injection method is its capability to be followed by subsequent electrophoretic deposition, which results in film deposition on an electrode from colloidal dispersions.[18] In fact, various films of the aggregated fullerene nanoclusters have been fabricated using this rapid injection-electrophoretic deposition protocol.[15,18] Considering that the integrative properties of film state is more informative than respective properties

† Part of the "Michael R. Wasielewski Festschrift".

* To whom correspondence should be addressed. E-mail: (H.I.) imahori@scl.kyoto-u.ac.jp; (S.S.) seki@chem.eng.osaka-u.ac.jp.

‡ Department of Molecular Engineering, Graduate School of Engineering, Kyoto University.

§ Department of Material Chemistry, Graduate School of Engineering, Kyoto University.

|| Tampere University of Technology.

⊥ Osaka University.

PRESTO, Japan Science and Technology Agency.

∇ Institute for Integrated Cell-Material Sciences (iCeMS), Kyoto University.

◆ Fukui Institute for Fundamental Chemistry, Kyoto University.

10.1021/jp911141s
Published on Web 02/05/2010

of nanocluster itself in terms of device application including BHJ solar cells, the ability to fabricate homogeneous thin films affords a substantial benefit. In addition, this protocol can be completed within a few minutes under an ambient atmosphere. Obviously, the simplicity and convenience of the rapid injection-electrophoretic deposition protocol to prepare fullerene-based films are advantageous over other preparation methods of fullerene assemblies, for instance, reprecipitation technique[3d,10e,11f] and liquid−liquid interfacial precipitation (LLIP),[6,7c,8b–d] which are regarded as useful methods to prepare the crystalline assemblies of fullerenes with varying shapes. In those methods, fullerene crystals are obtained as gradually growing precipitates. Thus, there is no chance for one-pot fabrication of thin films with sufficient uniformity by the following electrophoretic deposition. In this context, it can be affirmed that the rapid injection-electrophoretic deposition methodology is most suitable for systematic investigation on the photoelectrochemical properties of thin films composed of the fullerene assemblies.

In contrast to the reprecipitation, LLIP and other methodologies, the rapid injection technique typically affords fullerene aggregates with spherical shapes, which are difficult to be altered.[15–18] This always happens when C_{60} and its derivatives are used, as has been intensively studied by several groups.[15b,c,17b–f,18] On the other hand, the low symmetrical molecular structure of C_{70} leads to aggregation behavior different from C_{60}. Nath and co-workers have reported that C_{70} clusters prepared by the rapid injection method can vary its shape depending on the preparation condition, that is, fullerene concentration or solvents.[19] In their study, spherical[19a] and rodlike[19b] structures of C_{70} aggregates have been obtained by varying the concentration of C_{70} in benzonitrile prior to mixing with acetonitrile, or varying the volume ratio of benzonitrile and acetonitrile. However, photoelectrochemical investigations on the deposited films of the different-shaped clusters have not been conducted in the study. In addition, there still exists a possibility of further shape modulation of C_{70} aggregates. Given that the shape of the fullerene assemblies can be controlled by selecting the appropriate solvents in the cases of reprecipitation, LLIP and other methods,[3–11] it is reasonable to presume that the cluster shape can be also modulated by selecting the good solvent for the rapid injection method. Recently, we fabricated C_{70} cluster films electrophoretically deposited on the nanostructured SnO_2 electrodes from mixed solvents of toluene-acetonitrile[15a] and *o*-dichlorobenzene-acetonitrile.[20] We found a notable difference in the photocurrent generation efficiencies as well as in the film surface structures of the two electrodes modified with different C_{70} clusters. This is sharp contrast with similar spherical shapes and comparable photocurrent generation efficiencies for the cases of the clusterization of C_{60} in toluene-acetonitrile and *o*-dichlorobenzene-acetonitrile.[15,18] However, the underlying correlation between the photoelectrochemical properties and the cluster structures of C_{70} as well as the resultant film morphologies has remained unclear.

Here we report the first systematic studies on the electrophoretically deposited film structures, photoelectrochemical properties, and charge carrier mobilities of C_{70} clusters with different shapes (i.e., particles, rods, and plates) prepared by rapid injection method. The successful morphology engineering of the clusters was accomplished by changing the good solvents, in which C_{70} was dissolved before injection of acetonitrile (poor solvent). Morphologies of cluster and the resulting film were correlated with the photocurrent generation in terms of the light-absorption, carrier generation, and carrier transport properties by using various experimental techniques including the time-resolved microwave conductivity and transient absorption measurements. The charge carrier mobility is found to be the most predominant factor determining the photocurrent generation efficiency.

Experimental Section

General Procedures. UV−vis−near-infrared (NIR) absorption spectra of solutions and films were recorded on a Perkin-Elmer Lambda 900 UV/vis/NIR spectrometer. Field emission scanning electron microscopy (FE-SEM) observation was carried out with a JEOL JSM-6705F. For preparation of the cluster samples, a mixture of good solvent-acetonitrile containing C_{70} was spin-coated on Si wafer (polished wafer; SUMCO TECHX-IV) at a rotation speed of 1200 rpm. Prior to the observation, both spin-coated samples and electrophoretically deposited films were coated with 5 nm thick Pt layer using a JEOL JFC-1600 auto fine coater. Dynamic light scattering (DLS) measurements of the cluster solutions were performed by a Horiba LB550 particle size analyzer. Atomic force microscopy (AFM) images were obtained with a KEYENCE VN-8000 hybrid microscope in the tapping mode. Thickness of the deposited film was estimated by averaging the height of steps (over 80 points) at intentionally grooved trenches. X-ray diffraction (XRD) analyses were conducted on a Rigaku A2 diffractometer using Cu K_α radiation. X-ray photoelectron spectroscopy (XPS) on film samples was carried out with a SHIMADZU ESCA750S electron spectrometer. C_{60} (99.98%) and C_{70} (99.5%) were purchased from MTR Ltd. and used as-received. An optically transparent fluorine-doped tin oxide electrode (denoted as FTO; Asahi Glass) was washed by sonication in 2-propanol and cleaned in an O_3 atmosphere in advance. A 15% SnO_2 colloidal solution (particle size = 15 nm; Chemat Technology, Inc.) was deposited on the FTO electrode using doctor blade technique.[15c,20] The electrode was annealed at 673 K (denoted as FTO/SnO_2) to yield 0.5 μm thick SnO_2 film. All of the solvents employed (benzene, toluene, *o*-xylene, chlorobenzene, *o*-dichlorobenzene, benzonitrile, nitrobenzene, and anisole as a good solvent, and acetonitrile as a poor solvent) were of reagent-grade quality, purchased commercially, and used without further purification.

Solubility Evaluation of C_{70}. Solubility of C_{70} in various good solvents was estimated by using predetermined molar absorptivity of C_{70} and the absorbance of the saturated solution of C_{70} in the respective solvents.[21] Saturated solution was prepared by suspending excess C_{70} (~40 mg) in 2 mL of neat solvent by vigorous bath-sonication for 2 h then removing undissolved sediment by Millipore Millex-FG (pore size: 0.20 μm) syringe-driven filter unit. For accurate measurement of the absorption spectrum, the saturated solution was diluted appropriately with known amount of neat solvent.

Preparation of Cluster Solutions and Films. The cluster solutions of C_{70} (0.14 mM) were prepared in a 1 cm cuvette by quickly injecting 1.6 mL of acetonitrile into a solution of C_{70} (0.68 mM) in 0.4 mL of good solvent (good solvent/acetonitrile = 1:4 (v/v)).[20] Then, two electrodes (i.e., FTO and FTO/SnO_2) were inserted into the cuvette with keeping at a distance of 0.6 cm by a Teflon spacer. A DC voltage (200 V) was applied for 120 s between these two electrodes using a power supply (ATTO model AE-8750). The deposition of the film could be visibly confirmed as the suspension became colorless with simultaneous colorization of the FTO/SnO_2 electrode. After the deposition, the deposited film was dried immediately with a hair dryer. Likewise, the clusters of C_{60} (denoted as $(C_{60})_m$) were also prepared for the control experiments.

Photoelectrochemical Measurements. All electrochemical measurements were carried out in a standard three-electrode system using an ALS 630A electrochemical analyzer.[15c,20] The deposited film as a working electrode was immersed into an electrolyte solution containing 0.5 M LiI and 0.01 M I_2 in acetonitrile. A Pt wire covered with a glass Luggin capillary, whose tip was located near the working electrode, was used as a quasi-reference electrode. A Pt coil was employed as a counter electrode. The potential measured was converted to the saturated calomel electrode (SCE) scale by adding +0.05 V. A 500 W xenon lamp (XB-50101AAA; USHIO) was used as a light source. Potential versus current characteristics were measured with controlled-potential scan (1 mV s^{-1}) under 0.5 Hz chopped white light ($\lambda > 380$ nm; input power, 37 mW cm^{-2}). The light was passed through a monochromator (MC-10N; Ritsu) and focused on the modified area of the working electrode (0.20 cm^2) from the backside. The light intensity was monitored by an optical power meter (ML9002A; Anritsu), and the corrected values were used for calculation of incident photon-to-current efficiencies.

BET Surface Area Analyses. BET surface areas of the deposited film samples were obtained with a BEL JAPAN BELSORP28SA according to the nitrogen adsorption protocol at 77 K. Appropriately cut FTO/SnO_2 electrodes with deposited cluster films were inserted in the sample tube and dried under reduced pressure (<10^{-3} Torr) for 3 h before the measurements. The contribution from the bare FTO/SnO_2 electrode was subtracted from the whole surface areas and the specific surface areas of the deposited films were calculated based on the mass of C_{70} used for the film formation (0.23 mg).

Time-resolved Microwave Conductivity Measurements. Nanosecond laser pulses from a Nd:YAG laser (Spectra Physics, INDY-HG, third harmonic generation (THG), 355 nm) with full width at half-maximum (fwhm) of 3−5 ns were used as excitation sources. The photon density of the laser was set at 3.3×10^{15} photons cm^{-2}. For the time-resolved microwave conductivity (TRMC) measurements, a microwave frequency of 9.1 GHz and a power of 3−20 mW were employed so that the motion of charge carriers could not be disturbed by the low electric field of the microwaves. The TRMC signal, picked up by a diode (rise time < 1 ns), was monitored by a digital oscilloscope (Tektronix, TDS3032B, rise time ~1.2 ns). All the experiments were carried out at room temperature. The transient photoconductivity ($\Delta\sigma$) of the samples is related to the reflected microwave power ($\Delta P_r/P_r$) and the sum of the mobility of charge carriers via eqs 1 and 2

$$\langle \Delta\sigma \rangle = \frac{1}{a}\frac{\Delta P_r}{P_r} \quad (1)$$

$$\Delta\sigma = e\sum \mu\phi N \quad (2)$$

where a is the sensitivity factor, e is the elementary charge of electron, ϕ is the carrier generation efficiency, N is the number of absorbed photons per unit volume, and $\Sigma\mu$ is the sum of the mobility of all the transient charge carriers. The number of photons absorbed by the sample was estimated based on the power loss of incident laser pulses averaged over 200 shots. The ϕ values were determined by the conventional DC current integration technique. The electrophoretically deposited films were overcoated by Au semitransparent electrodes at 20 mm^2, vacuum evaporated to a thickness of 25 nm, and excited by laser pulses at 355 nm with a pulse duration of 3−5 ns and a photon density of 3.0×10^{15} photons cm^{-2}. Current transients were monitored by a digital oscilloscope (Tektronix, TDS430A) through 300 kΩ terminate resistances, and the charges were also accumulated by an electrometer of Keithley Instruments 6514. Other details of the apparatus set are described elsewhere.[22]

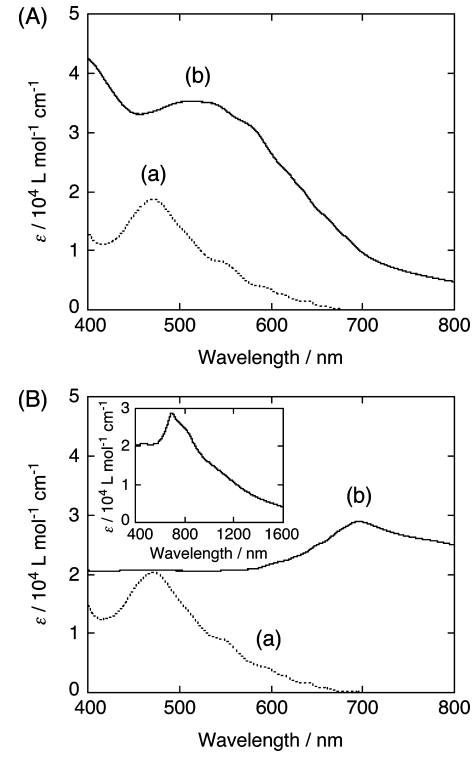

Figure 1. (A) UV−vis−NIR absorption spectra of C_{70} measured in (a) BZ ([C_{70}] = 0.68 mM; path length, 1 mm) and (b) BZ-AN mixture (1:4 (v/v); [C_{70}] = 0.14 mM; path length, 3 mm). (B) UV−vis−NIR absorption spectra of C_{70} measured in (a) DCB ([C_{70}] = 0.68 mM; path length, 1 mm) and (b) DCB-AN mixture (1:4 (v/v); [C_{70}] = 0.14 mM; path length, 3 mm). Inset shows spectrum (b) with wider wavelength range.

Spectral Measurements. A pump−probe method was used to measure transient absorption spectra in subpicosecond to nanosecond time domain. The measurements were carried out using the instrument described previously.[23] Briefly, the transient spectra were recorded by a CCD detector coupled with a monochromator in the visible and near-infrared ranges and the second harmonic (410 nm) of Ti:sapphire laser was used for the excitation. A typical time resolution of the instrument was 150 fs (fwhm) and the details are described in the Supporting Information.

Results and Discussion

Spectroscopic Characterization on Clusterization of C_{70}. The C_{70} cluster solution (0.14 mM) was prepared by rapidly injecting acetonitrile (denoted as AN, poor solvent) into a solution of C_{70} dissolved in various good solvents (0.68 mM). For the good solvent, we chose benzene (denoted as BZ), toluene (TL), *o*-xylene (XY), chlorobenzene (CB), *o*-dichlorobenzene (DCB),[20] benzonitrile (BZN), nitrobenzene (NB), and anisole (ANS), all of which have reasonably high solubilities for C_{70} ranging from 1.5 mM for BZ to 43 mM for DCB (see Supporting Information Table S1). For all the solvent combinations, volume ratio of good solvent-acetonitrile (1:4) and C_{70} concentration (0.14 mM in the mixed solvents) were kept constant.[24] The clusterization behaviors of C_{70} in the solvent mixtures were first investigated by using UV−vis−NIR absorption spectroscopy. Figure 1A illustrates the UV−vis−NIR

absorption spectra measured in BZ (trace a) and BZ-AN mixture (trace b). In neat BZ, the absorption feature with maximum at 470 nm and shoulders around 550−680 nm agrees well with the characteristics of the monomeric C_{70} absorption.[25] In BZ-AN mixture, the intense peak around 470 nm observed in neat BZ solution is red shifted to ∼520 nm and significantly broadened exhibiting an absorption tail extending to NIR region (> 800 nm). Such a drastic change in the absorption spectrum is ascribed to the formation of clusterized species of C_{70} (denoted as $(C_{70})_m$) due to the lyophobic interaction between the mixed solvent and C_{70} molecules in addition to the $\pi-\pi$ interaction between C_{70} molecules, as reported by several groups.[16,17a,g,19] Likewise, absorption spectra in other neat solvents (BZN, NB, TL, CB, and ANS) reveal monomeric features of C_{70} and the spectral changes largely similar to Figure 1A are discernible upon injection of AN (Supporting Information Figure S1A−E). Thus, C_{70} exists as its monomeric form without AN and as cluster form with AN in these solvents. On the other hand, albeit the absorption spectra in DCB and XY display typical monomer characteristics, those in DCB-AN[20] and XY-AN mixtures disclose totally different features from the behavior in other mixed solvents (Figure 1B and Supporting Information Figure S1F). Namely, the intense peak at 470 nm observed in neat solvents disappears and a new broad band around 700 nm emerges with retaining absorption over 1600 nm. Taking into account the high solubilities of C_{70} in DCB and XY as good solvents relative to the other good solvents, DCB and XY molecules may interact so strongly with C_{70} molecules as to be incorporated into $(C_{70})_m$ upon the clusterization in the mixed solvents. The incorporated solvents would affect the local environments of $(C_{70})_m$, altering the electronic structure of C_{70} and/or the electronic coupling interaction between C_{70} molecules within the cluster.

Microscopic Observations of C_{70} Clusters. Field emission scanning electron microscopy (FE-SEM) measurements were conducted to evaluate the structures of the $(C_{70})_m$ (Figure 2 and Supporting Information Figure S2). The samples for the FE-SEM observations were prepared by spin-coating the cluster solutions onto silicon wafer. In parallel, dynamic light scattering (DLS) measurements were also performed to complement the FE-SEM results (Supporting Information Figure S3). The FE-SEM image of $(C_{70})_m$ prepared from BZ-AN mixture reveals granular aggregates with a size of ∼250 nm (Figure 2a). Correspondingly, DLS measurement of the cluster solution in BZ-AN shows a monomodal size distribution with an average diameter (D_{av}) of 240 nm (Supporting Information Figure S3A(a)). Likewise, $(C_{70})_m$ formed in BZN-AN (Figure 2b) and NB-AN (Supporting Information Figure S2a) are found to be granular aggregates with sizes of ∼170 and ∼180 nm, which are consistent with the D_{av} values obtained from the DLS measurements (Supporting Information Figure S3A(b,c)). In contrast, Figure 2c displays rodlike structures of $(C_{70})_m$ prepared from TL-AN mixture with lengths of 200−400 nm, accompanying small particles with a diameter of ∼100 nm.[26] The FE-SEM image of $(C_{70})_m$ formed in CB-AN exhibits analogous rodlike assemblies with sizes of 200−500 nm in length (Figure 2d). DLS measurements on the cluster solutions in TL-AN and CB-AN show rather broad distributions with D_{av} of 230 and 290 nm, respectively, which agree with the FE-SEM observations (Supporting Information Figure S3B(a,b)). On the other hand, the FE-SEM image of $(C_{70})_m$ prepared from ANS-AN mixture depicts fragile, platelike structures with sizes over 1 μm (Figure 2e). Consistently, DLS experiment on the cluster solution exhibited bimodal broad distribution with maxima at 340 nm and ∼2.5 μm, which may be correlated with the platelike structures with the large aspect ratio of the thin thickness and the large two-dimensional size (Supporting Information Figure S3B(c)). To the best of our knowledge, this is the first example of the platelike cluster of C_{70} prepared by the rapid injection method. Figure 2f illustrates cuboidal particles of $(C_{70})_m$ formed in DCB-AN mixture with sizes of 260−360 nm, which is in good agreement with D_{av} of 330 nm estimated from DLS (Supporting Information Figure S3C(a)).[20] Similar cuboidal particles (Supporting Information Figure S2b) are observed for $(C_{70})_m$ prepared from XY-AN (D_{av} = 170 nm, Supporting Information Figure S3C(b)). Thus, emphasis should be placed on the successful cluster morphology engineering of $(C_{70})_m$ by altering the good solvents, affording particulate, rodlike, and platelike structures with controllable size distributions ranging from ∼100 nm to over micrometer scale. It should be noted here that various other factors, such as the volume ratio of good and poor solvents, concentration, and poor solvent used, would also influence the cluster morphology prepared by the rapid injection. In fact, it was reported by Nath and co-workers that BZN-AN could selectively afford both spherical particles and rod-like aggregates of C_{70} depending on the volume ratio of the solvents (volume (%) of AN < 75% for sphere and > 75% for rod, respectively) at relatively low concentration ($[C_{70}]$ = 0.0126 mM).[19] Although more detailed, extensive studies on the cluster morphology engineering are necessary, we can conclude that intermolecular interaction between C_{70} molecules and good solvents at least has a large impact on the shape and size of $(C_{70})_m$ clusters prepared by the rapid injection method.

Of another interest to note here is the correlation between the cluster shapes and the absorption spectra. For instance, the absorption spectra of $(C_{70})_m$ prepared in BZ-AN, BZN-AN, NB-AN, TL-AN, CB-AN, and ANS-AN reveal similar spectral features as represented by Figure 1A(b), despite the remarkable variation of the cluster shapes and sizes. This result implies resemblance in the microscopic environments surrounding C_{70} molecules in the respective clusters, although the eventual cluster shapes are not necessarily the same. Moreover, the notably different absorption spectra of $(C_{70})_m$, prepared in DCB-AN as well as XY-AN, from those prepared in the other good solvent-AN mixtures, may result from the altered electronic states of C_{70} induced by the different local environments around C_{70} molecules in the clusters incorporating the good solvents (vide supra), whereas the difference does not have correlation with their shape of cuboidal clusters.

Electrophoretic Deposition. For the photoelectrochemical measurements and the other experiments, the clusters of C_{70} were electrophoretically deposited onto nanostructured SnO_2 electrodes from the corresponding solvent mixtures (denoted as FTO/SnO_2/$(C_{70})_m$). Under an application of the high DC electric field (200 V), the clusters, which were negatively charged in the mixed solvent, were driven toward the positively charged electrode (i.e., FTO/SnO_2). The film formation was probed by monitoring the changes in absorbance of the electrophoretically deposited electrodes as a function of the deposition time. The film formation reached completion within 120 s for all cases. Hence, we used electrodes prepared with the deposition time of 120 s for all the following measurements.

Absorption Spectroscopy of the Deposited Films. The UV−vis−NIR absorption spectra of the FTO/SnO_2/$(C_{70})_m$ electrodes are shown in Figure 3 and Supporting Information Figure S4. Apparently, all of the modified electrodes exhibit analogous spectra with noticeable shoulder around 500 nm, which are largely similar to those of the typical cluster solution

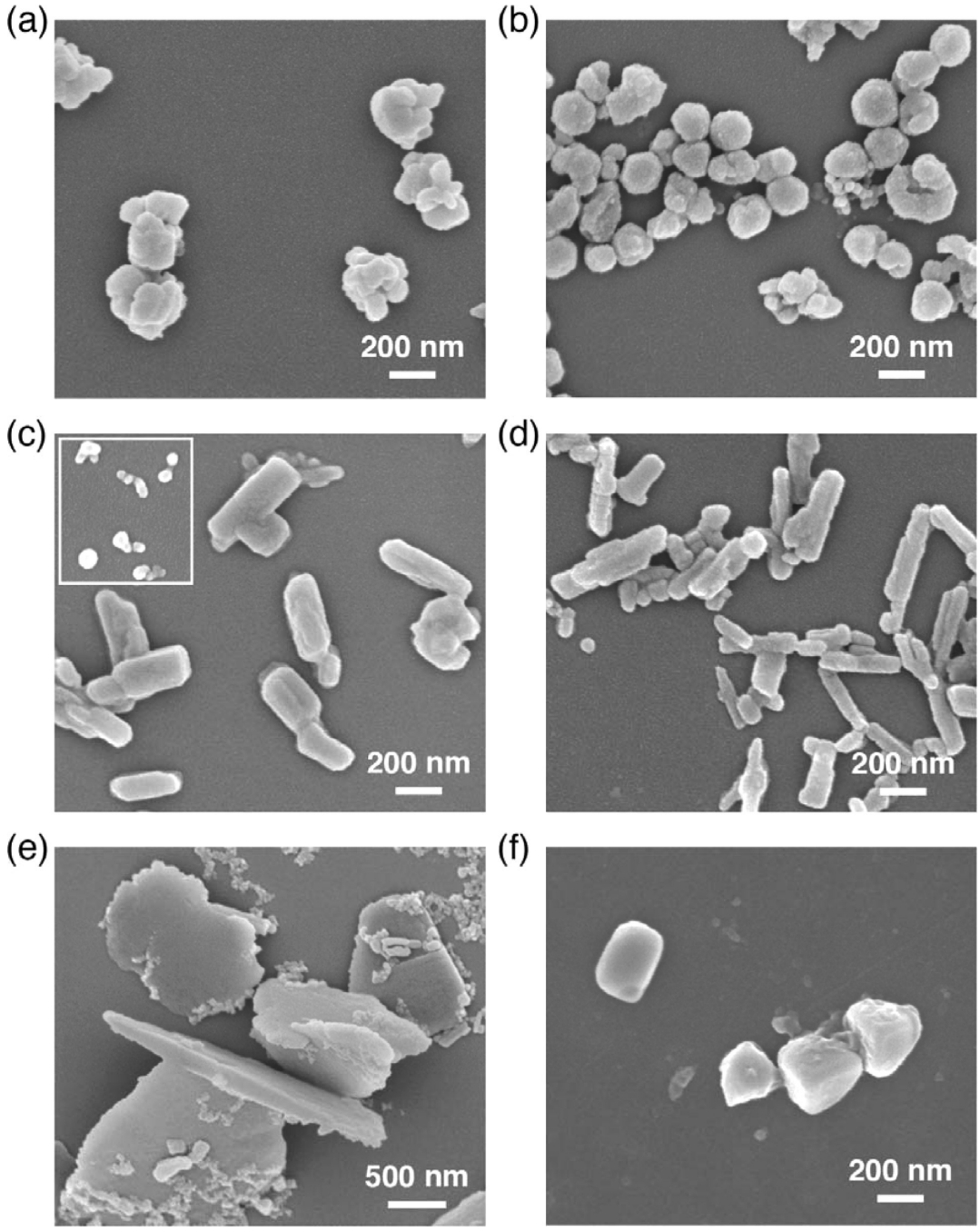

Figure 2. FE-SEM images of $(C_{70})_m$ prepared from mixed solvents of (a) BZ-AN, (b) BZN-AN, (c) TL-AN, (d) CB-AN, (e) ANS-AN, and (f) DCB-AN. The samples were spin-coated on Si wafer from corresponding cluster solutions (good solvent/AN = 1:4 (v/v); $[C_{70}] = 0.14$ mM). Inset in Figure 2c shows particulate clusters observed at different site on the same substrate.

(Figure 1A(b)). It is noteworthy that the absorption spectra of the electrodes deposited from DCB-AN[20] (Figure 3d) and XY-AN (Supporting Information Figure S4d) are different from those of the respective cluster solutions. Namely, the broad absorption around 700 nm observed in the cluster solutions disappeared and the prominent shoulder at 450−700 nm became apparent. Such a spectral change is indicative of the structural alteration of $(C_{70})_m$ on the electrodes (vide infra). Note that the position of the absorption maximum at 480 nm in the case of FTO/SnO_2/$(C_{70})_m$ electrodes prepared from DCB-AN is close to that of the characteristic peak at 470 nm arising from the monomeric C_{70} (Figure 1B(a)). The broad absorption of these films as well as their high absorption in the visible region makes these films suitable for harvesting solar energy.

Surface Characterization of the Deposited Films. FE-SEM was employed to evaluate the surface morphology of the electrophoretically deposited films (Figure 4 and Supporting Information Figure S5). The FE-SEM image of the FTO/SnO_2/$(C_{70})_m$ electrode prepared from BZ-AN (Figure 4a) shows densely packed particles with sizes of 100−250 nm, which resemble those observed in the spin-coated sample (Figure 2a). Thus we conclude that the $(C_{70})_m$ formed in the mixed solvent was successfully deposited onto the FTO/SnO_2 electrode without significant change in its structure. Similarly, FTO/SnO_2/$(C_{70})_m$ electrodes, prepared from BZN-AN (Figure 4b), TL-AN (Figure 4c), CB-AN (Figure 4d), ANS-AN (Figure 4e), and NB-AN (Supporting Information Figure S5a), exhibit closely packed clusters that are virtually the same as those observed in the

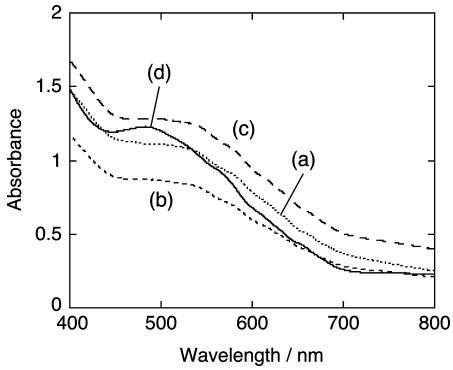

Figure 3. UV−vis−NIR absorption spectra of FTO/SnO_2/$(C_{70})_m$ electrodes prepared by electrophoretic deposition from cluster solutions of C_{70} in (a) BZ-AN, (b) TL-AN, (c) CB-AN, and (d) DCB-AN mixtures.

corresponding FE-SEM images of the spin-coated samples. In contrast, FTO/SnO_2/$(C_{70})_m$ electrode, deposited from DCB-AN mixture, discloses blurred structureless surface morphology from which small grains are protruded (Figure 4f).[20] The cuboidal clusters observed in the spin-coated sample (Figure 2f) are totally absent. Given the fact that the absorption spectral shape of the deposited film is close to that arising from the monomeric C_{70} in DCB rather than that arising from the $(C_{70})_m$ in DCB-AN mixture (vide supra), it is most likely that the aggregated state of C_{70} is transformed into the monomeric C_{70} on the electrode, yielding an amorphous-like film with granulous remnants of aggregated C_{70}.[20] Meanwhile, the FE-SEM image of FTO/SnO_2/$(C_{70})_m$ electrode prepared from XY-AN depicts unique nanostructures protruding from the bottom of the SnO_2 electrode (Supporting Information Figure S5b). Note that the angular-shaped particles observed on Si wafer (Supporting Information Figure S2b) are not seen. These micrographic observations together with the spectroscopic change upon electrophoretic deposition (Supporting Information Figures S1F and S4d) obviously manifest the regeneration of C_{70} monomers from C_{70} aggregate. Such behavior of $(C_{70})_m$ may be explained by the extraordinary high solubility of C_{70} in DCB and XY (Supporting Information Table S1), as well as the difference in boiling points (bp) of good and poor solvents. That is, during drying process of the deposited electrode by dryer, AN with low bp of 82 °C vaporizes much faster than DCB with high bp of 180 °C and XY with high bp of 143 °C. The resultant good solvent-rich environment on the electrode would dissociate aggregated C_{70} to regenerate the monomeric C_{70} without especial stimulation like sonication, owing to the high solubilities of C_{70} in DCB and XY. Furthermore, the vaporization of solvent molecules incorporated in the clusters may facilitate the collapse of the cuboidal clusters. The dissolution of aggregated C_{70} did not occur in the cases of BZN-AN and NB-AN systems, where good solvents possess even higher bp (BZN, 191 °C; NB, 210 °C), but exhibit one-order lower solubilities of C_{70} in BZN and NB than in DCB and XY.

The structures of $(C_{70})_m$ on the FTO/SnO_2 electrodes are summarized in Table 1. It is expected that the morphological difference of the fabricated films, as well as the morphological change upon electrophoretic deposition in the cases of DCB-AN and XY-AN systems, should affect the photoelectrochemical properties.

Photoelectrochemical Properties. Photoelectrochemical measurements were performed in deaerated acetonitrile containing 0.5 M LiI and 0.01 M I_2 with the FTO/SnO_2/$(C_{70})_m$ electrodes as a working electrode, a platinum wire as a counter electrode, and an I^-/I_3^- reference electrode. Figure 5a displays representative photocurrent response of the electrode prepared from BZ-AN mixture illuminated with white light ($\lambda > 380$ nm) at an applied potential of 0.05 V versus SCE. The photocurrent response is prompt, steady, and reproducible during the repeated on/off cycles of the visible light illumination. Blank experiment of the FTO/SnO_2 electrode without deposited films exhibited negligible photocurrent responses under the same conditions, demonstrating the role of the deposited clusters toward harvesting light energy and generating electron flow from the electrolyte to the FTO/SnO_2 electrode through the film. Figure 5b illustrates current versus potential curve of the same device. With increasing positive bias up to 0.05 V versus SCE, the photocurrent is increased compared to the dark current. The increased charge separation and the facile transport of the generated charge carriers under positive bias are responsible for the enhanced photocurrent generation. Similar photoelectrochemical behaviors were observed for the other FTO/SnO_2/$(C_{70})_m$ electrodes.

For further insights into the photoelectrochemical properties of the deposited films, we evaluated the wavelength dependent incident photon-to-current efficiency (IPCE) spectra. The IPCE values are calculated by normalizing the photocurrent densities for incident light energy and intensity and by use of the expression

$$\mathrm{IPCE}\ (\%) = 100 \times 1240 \times i/(W_{\mathrm{in}} \times \lambda)$$

where i is the photocurrent density (A cm^{-2}), W_{in} is the incident light intensity (W cm^{-2}), and λ is the excitation wavelength (nm).

Figure 6 depicts the photocurrent action spectra of the FTO/SnO_2/$(C_{70})_m$ electrodes. The photocurrent action spectra largely parallel the absorption spectra of the deposited electrodes (Figure 3 and Supporting Information Figure S4). The IPCE values are compared at 400 nm where the values are maximal and most of the incident light is absorbed by the films (Table 1). The maximum IPCE (10%)[20] of the electrode prepared from DCB-AN mixture outperforms the corresponding values of the electrodes prepared from NB-AN (4.8%), BZ-AN (4.6%), BZN-AN (4.5%), ANS-AN (2.5%), TL-AN (1.7%), XY-AN, (1.0%), and CB-AN (0.82%) mixtures. Considering the sufficiently high light-harvesting property at 400 nm (absorbance > 1), the difference in the maximum IPCE values originates from those in charge separation efficiency and charge collection efficiency (vide infra).[27] We emphasize that the different shapes of $(C_{70})_m$, thereby different morphologies of the electrophoretically deposited films, lead to different photocurrent generation efficiencies ranging from 0.8 to 10%. This is in stark contrast to the results for C_{60} clusters prepared by the same rapid injection method, where spherical assemblies are formed irrespective of the clusterization conditions and maximum IPCE around 3−5% are obtained when the clusters are deposited onto the SnO_2 electrodes.[15,18,28]

Photocurrent Generation Mechanism. Before focusing the correlation between the film morphologies and the photoelectrochemical properties, we present the photocurrent generation mechanism of the FTO/SnO_2/$(C_{70})_m$ electrodes on the basis of the previously studied C_{60}-based devices (Scheme 1).[15,18]

Photocurrent generation is initiated by absorption of the incident light by C_{70} (step 1), yielding the highly energetic excited states of C_{70} (lowest singlet energy, ~1.9 eV; lowest triplet energy, ~1.5 eV).[29] Then, electron transfer (ET) from iodide ion ($I_3^-/I^- = 0.5$ V vs NHE)[15,18] in the electrolyte to the excited C_{70} ($^1C_{70}^*/C_{70}^{\bullet-} \approx 1.7$ V vs NHE; $^3C_{70}^*/C_{70}^{\bullet-} \approx 1.3$ V

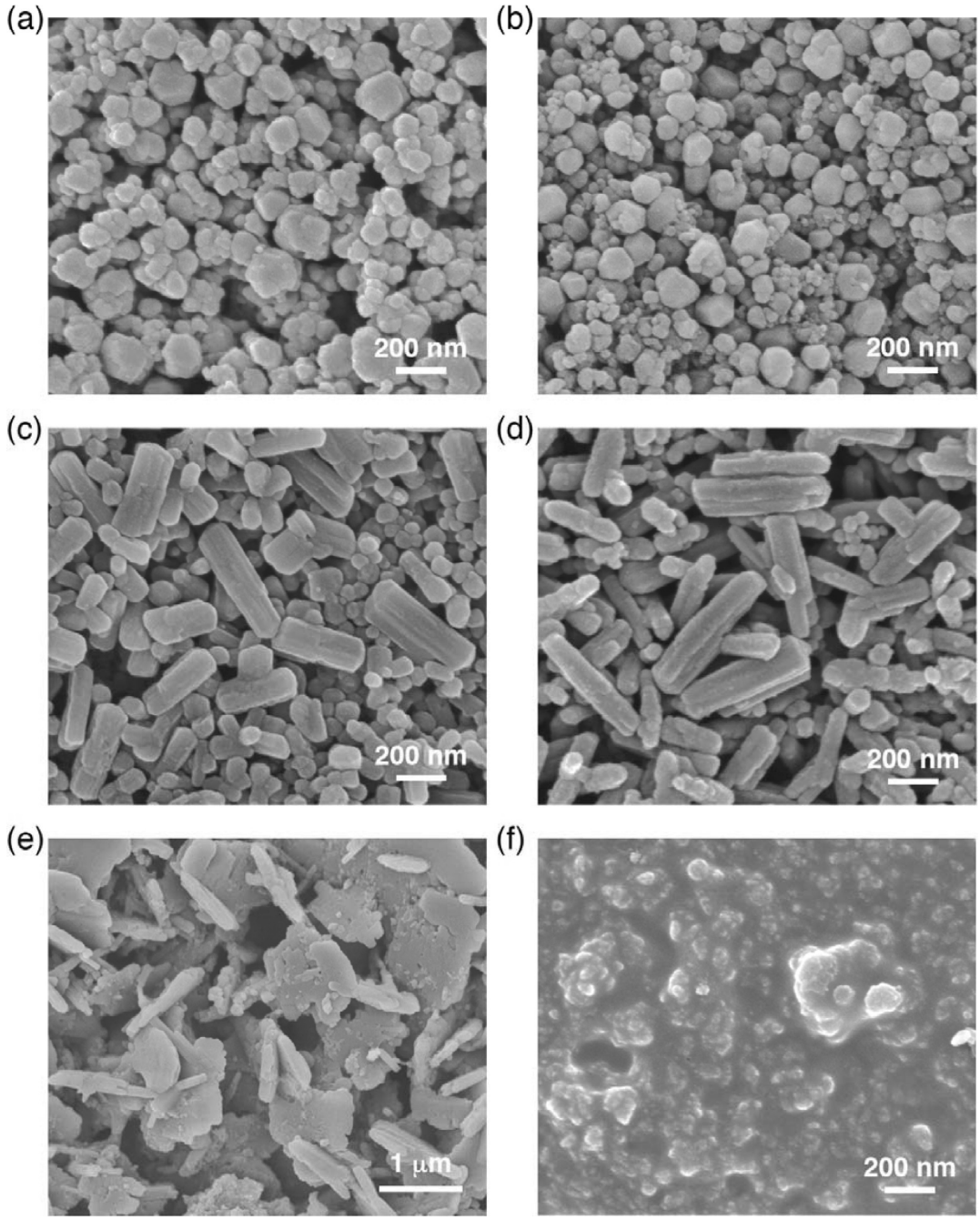

Figure 4. FE-SEM images of FTO/SnO_2/$(C_{70})_m$ electrodes prepared from mixed solvents of (a) BZ-AN, (b) BZN-AN, (c) TL-AN, (d) CB-AN, (e) ANS-AN, and (f) DCB-AN. All samples were coated with ca. 5 nm thick Pt layer prior to the measurements.

TABLE 1: Cluster Structure, IPCE Value, Surface Area, Film Thickness, and Electron Mobility of FTO/SnO_2/$(C_{70})_m$ Electrodes Prepared from Various Solvent Mixtures

solvent	structure of $(C_{70})_m$	IPCE at 400 nm/%	surface area[a]/m^2 g^{-1}	film thickness[b]/nm	$\Sigma\mu$[c]/cm^2 V^{-1} s^{-1}
o-dichlorobenzene (DCB)-AN	amorphism[d]	10	22	400 ± 130	1.9[e]
nitrobenzene (NB)-AN	particle	4.8	58	700 ± 210	0.38
benzene (BZ)-AN	particle	4.6	88	830 ± 310	0.21
benzonitrile (BZN)-AN	particle	4.5	114	670 ± 240	0.15
anisole (ANS)-AN	plate	2.5	50	1450 ± 260	0.098
toluene (TL)-AN	rod + particle[f]	1.7	65	680 ± 230	0.048
o-xylene (XY)-AN	protruding structure[g]	1.0	69	820 ± 530	0.037
chlorobenzene (CB)-AN	rod	0.82	87	560 ± 170	0.043

[a] Calculated by subtracting the contribution from the bare FTO/SnO_2 electrode. [b] Determined by subtracting thickness of SnO_2 base layer (~540 nm) from total thickness. [c] $\Sigma\mu$: sum of mobilities of all the transient-charge carriers calculated by maximum value of transient conductivity upon photoexcitation at 355 nm and quantum efficiency of carrier generation determined for DCB-AN sample (0.031) with conventional DC-current integration. [d] Rearranged from cuboidal particle. [e] From ref 20. [f] The ratio of rod and particle structures was estimated as ~1:2 from the FE-SEM image of deposited film. [g] Rearranged from angulated particle.

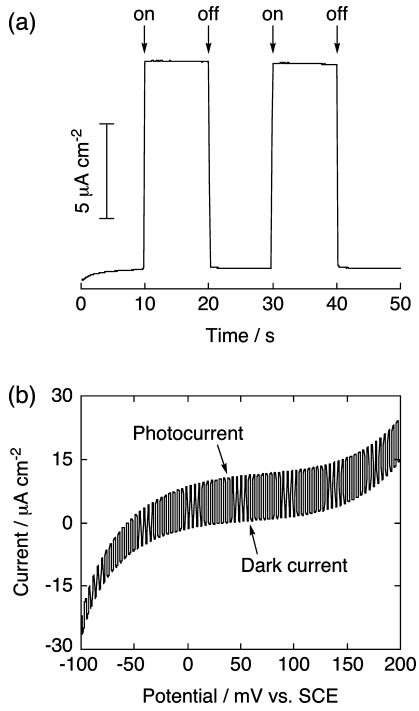

Figure 5. (a) Photocurrent response and (b) current vs potential curve of FTO/SnO_2/$(C_{70})_m$ electrode prepared from cluster solution in BZ-AN mixture. Illuminated with white light ($\lambda > 380$ nm; input power, 37 mW cm^{-2}); electrolyte: 0.5 M LiI and 0.01 M I_2 in acetonitrile. The photoresponse was measured under an applied potential of +0.05 V vs SCE.

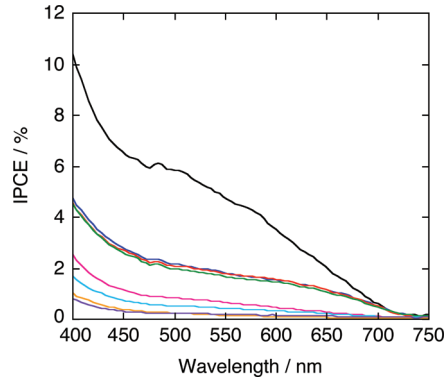

Figure 6. Photocurrent action spectra of FTO/SnO_2/$(C_{70})_m$ electrodes prepared from mixed solvents of, from top to bottom, DCB-AN (black), NB-AN (blue), BZ-AN (red), BZN-AN (green), ANS-AN (pink), TL-AN (light blue), XY-AN (orange), and CB-AN (purple). Applied potential: +0.05 V vs SCE; electrolyte: 0.5 M LiI and 0.01 M I_2 in acetonitrile.

vs NHE)[29,30] occurs as in the case of analogous photoelectrochemical devices utilizing C_{60} clusters (step 2).[15,18] Next, the reduced C_{70} ($C_{70}/C_{70}^{\bullet -} \approx -0.2$ V vs NHE)[30] mediates its electron toward the SnO_2 layer through the C_{70} arrays via electron hopping (step 3). Finally, C_{70} radical anion, which is closest to the SnO_2 surface, injects electron into the conduction band of SnO_2 ($E_{CB} = 0$ V vs NHE) (step 4).[15,18] The electrons injected into the SnO_2 electrode are driven to the counter electrode via external circuit to regenerate the redox couple. Thus, photocurrent generation mechanism is basically divided into four steps (steps 1−4) and the IPCE is a product of the efficiencies of the respective steps. Of these, step 1, that is, light absorption, is unlikely a key factor yielding the difference in the IPCE values (vide supra). Therefore, we have to consider the efficiencies of steps 2−4. As for step 2, the charge separation (CS) efficiency

SCHEME 1: Schematic Diagram of Photocurrent Generation in FTO/SnO_2/$(C_{70})_m$ Device

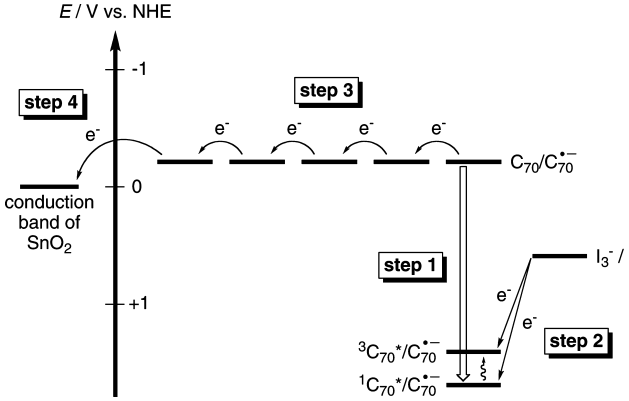

from I^- to the C_{70} excited states depends on the exciton diffusion lengths and lifetimes of the C_{70} excited states, the thickness and the surface area of the deposited films, and diffusion process of I^- to the C_{70} excited states at the interface of the film surface and the electrolyte solution. Assuming that the exciton diffusion lengths and the lifetimes of the C_{70} excited states and the diffusion process of I^- to the C_{70} excited states in the interface are similar in the present systems, the thickness and the surface area of the deposited films are responsible for difference in the CS efficiency of step 2.[31] The CS efficiency would increase if the film thickness becomes smaller or the surface area becomes larger, but the larger surface area may also induce the unfavorable carrier recombination between $C_{70}^{\bullet -}$ and I_3^-. On the other hand, the electron-transporting efficiency of step 3 would be enhanced as the film thickness is smaller or the electron mobility within the film is larger. Finally, the electron injection efficiency of step 4 can be discussed in terms of the reduction potential of C_{70}. Here, the reduction potential of C_{70} can be regarded as independent of the cluster structures.[18a] Therefore, surface area, film thickness, and electron mobility are the subjects of further investigation.

Surface Area and Film Thickness. The surface areas of the FTO/SnO_2/$(C_{70})_m$ electrodes were evaluated by BET analyses with N_2 adsorption protocol at 77 K. The BET surface area was calculated by subtracting the contribution from the bare FTO/SnO_2 electrode. It should be noted that the value determined for the film prepared from ANS-AN mixture represents the lower limits since the deposited film partially exfoliates after the electrophoretic process in this case.[27] The BET surface areas of the FTO/SnO_2/$(C_{70})_m$ electrodes are listed in Table 1 and plotted as a function of the maximum IPCE values (Figure 7). It is evident that there is no correlation between the two parameters. Thus, the surface area of the deposited films has no significant impact on the difference in the IPCE values.

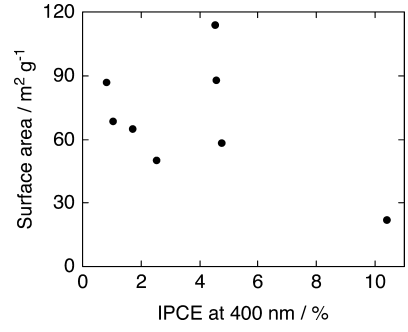

Figure 7. Plot of BET surface areas vs IPCE values at 400 nm.

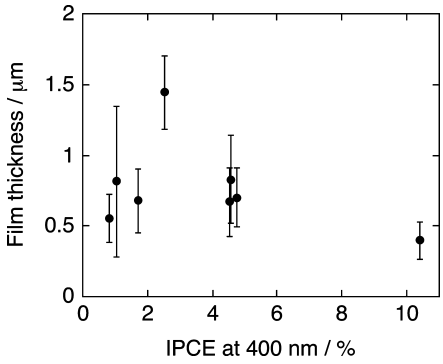

Figure 8. Plot of film thicknesses vs IPCE values at 400 nm. Error bar denotes the corresponding standard deviation of thickness.

The thickness of the deposited film was determined by analyzing the AFM height profile of the intentionally grooved trenches on the film (Supporting Information Figure S8). To assess the cluster layer only, average thickness of the SnO_2 layer (540 nm) was subtracted from that of the whole film. The thicknesses are summarized in Table 1 and plotted vs the maximum IPCE (Figure 8). There is no systematic change in the IPCE values as a function of the film thickness. Therefore, the film thickness is not a decisive parameter for the difference in the IPCE values. The alignment of C_{70} molecules in the cluster may influence more significantly the photocurrent generation efficiency (vide infra).

Transient Microwave Conductivity. Flash-photolysis time-resolved microwave conductivity (TRMC) measurements[22] were performed on the deposited films of $(C_{70})_m$ to evaluate the charge carrier mobility (μ). For the sample preparation, the films were peeled off from the FTO substrate and fixed on quartz plates with poly(methyl methacrylate) matrices. Upon exposure to a laser pulse with an excitation wavelength of 355 nm, all samples exhibit a rise of the transient conductivity $<\phi\Sigma\mu>$ in which ϕ is the quantum efficiency of charge carrier generation and $\Sigma\mu$ is the sum of the mobility of all the transient charge carriers (Figure 9A). The $\Sigma\mu$ values are calculated using the maximum values of $<\phi\Sigma\mu>$ and the ϕ value (0.031)[20] determined for the film prepared from DCB-AN mixture with conventional DC current integration technique, assuming that the ϕ value is independent of the cluster structures and the film morphologies. This assumption is likely to be reasonable considering the similarity of the excited state dynamics of the deposited films.[31] Additionally, it should be mentioned that the major charge carriers stem from electrons as indicated by effective accumulation of negative charges into the integrator under negative bias mode, whereas negligible positive charges are observed under positive bias mode. The $\Sigma\mu$ values are listed in Table 1 and the plot of the $\Sigma\mu$ values versus the maximum IPCE values is illustrated in Figure 9B.

Figure 9B manifests that the IPCE value is increased with increasing the $\Sigma\mu$ value. Thus, the electron-transporting process of step 3 turns out to have a large influence on the IPCE values in the present systems. The largest maximum IPCE value (10%) of the FTO/SnO_2/$(C_{70})_m$ electrode prepared from DCB-AN mixture mainly results from the remarkably high electron mobility (1.9 $cm^2\ V^{-1}\ s^{-1}$).

Then, one fundamental question arises: what factor determines the mobility?[32] This seems to be closely related to the packing pattern of C_{70} molecules in the respective clusters, as have been demonstrated in the previous study on porphyrin-C_{60} assembly.[2e,f,33] Given the fact that the TRMC mobilities are higher for the films with particulate clusters, prepared from BZ-AN, BZN-AN, and

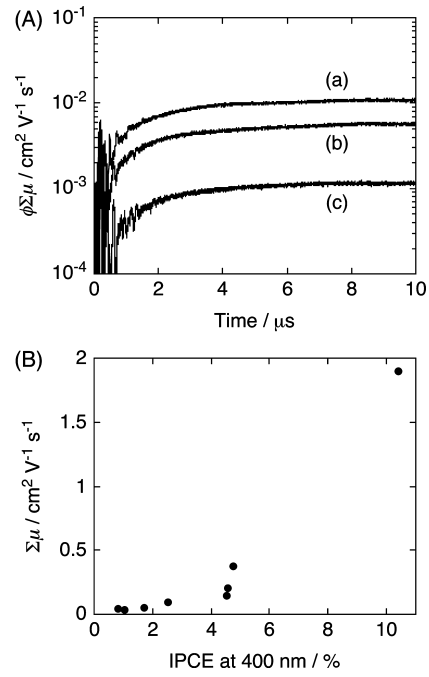

Figure 9. (A) Flash-photolysis time-resolved microwave conductivity transients for FTO/SnO_2/$(C_{70})_m$ electrodes prepared from mixed solvents of (a) NB-AN, (b) BZ-AN, and (c) CB-AN. The transient were recorded at an excitation wavelength of 355 nm with a photon density of 3.3×10^{15} cm^{-2}. All samples are fixed on quartz substrates with poly(methyl methacrylate) matrices. (B) Plot of microwave electron mobilities vs IPCE values at 400 nm.

NB-AN, than those for the films with rodlike clusters, prepared from TL-AN and CB-AN, and platelike clusters, prepared from ANS-AN, there seems to be connection among the cluster structure, molecular packing, and carrier mobility (Table 1). To shed light on the inner structures of $(C_{70})_m$, we conducted the XRD analyses on the cluster films. However, no XRD patterns arising from the crystalline packing of C_{70}[34] are observed for all the samples (Supporting Information Figure S9), indicating that any existing crystallites in $(C_{70})_m$ are too small to be detected or inner structures of $(C_{70})_m$ are rather amorphous.

The turnover period of the microwave is about ~110 ps at 9.1 GHz used in the TRMC measurement, suggesting the perturbation length of the negative charge carriers as ~2 nm with the values of observed mobilities (~0.5 $cm^2\ V^{-1}\ s^{-1}$), under the averaged strength of the employed electric field ($(3-4) \times 10^2$ V cm^{-1}). This implies that the TRMC measurements probe the AC-field induced oscillating motion of the electrons within a few molecules of C_{70}.[35] Hence, we could postulate that the tiny stacks comprised of several C_{70} molecules affects strongly the TRMC mobility and the eventual cluster shape, without showing observable signals in the XRD pattern.[17f,g,36] For instance, the small stacks of C_{70} molecules with desirable structure for the efficient electron hopping may lead to the spherical shaped clusters, while other types of stacks, which are undesirable for the efficient electron hopping, result in the rodlike or platelike clusters. In the case of the film deposited from DCB-AN, the melting behavior of the deposited clusters by the drying process would be responsible for the formation of favorable pathway for efficient electron hopping, whereas for the formation of unfavorable pathway in the film from XY-AN.

Conclusion

We have systematically examined the good solvent effects of C_{70} clusterization behavior in the good-poor solvent mixtures

as well as of their electron-transporting and photoelectrochemical properties for the first time. The successful cluster morphology engineering of C_{70} was achieved by changing the good solvent, affording the spherical, rod-like, and plate-like clusters. The C_{70} clusters were electrophoretically deposited onto the nanostructured SnO_2 electrodes and their photoelectrochemical properties were examined. The incident photon-to-current efficiency (IPCE) varied dramatically from 0.8 to 10% depending on the solvent combination for the cluster formation. The origin of the variation in the IPCE values was discussed in terms of the surface area, film thickness, and electron mobility. The electron mobility was found to be the most predominant factor for the difference in the IPCE values, implying the importance of the electron-transporting process in the C_{70} films. The underlying molecular packing and the resultant cluster structure were suggested to correlate with the electron mobility. Accordingly, these results will provide basic information on supramolecular chemistry of fullerenes as well as the design of the fullerene-based molecular devices including the organic photovoltaics.

Acknowledgment. H.I. thanks Grand-in-Aid from MEXT, Japan (Priority Area of Molecular Theory for Real Systems (No. 19029020) for financial support. N.T. thanks Research Fellowships of the Japan Society for the Promotion of Science (JSPS) for Young Scientists. T.U. thanks Kansai Research Foundation (KRF) for financial support. We thank Ms. Tomoyo Asada (Kyoto Univ.) for the FE-SEM observations, Mr. Tomoyuki Kitano and Mr. Toshio Uesaka (Kyoto University) for the BET analyses, and Professor Hironori Kaji and Mr. Tatsuya Fukushima (Kyoto University) for the attempt to conduct time-of-flight measurements on the films.

Supporting Information Available: Experimental details for time-resolved absorption spectroscopy, table of boiling point and C_{70} solubility, and figures for absorption spectra (S1), FE-SEM images (S2) and particle size distributions (S3) of $(C_{70})_m$, absorption spectra (S4) and FE-SEM images (S5) of FTO/SnO_2/$(C_{70})_m$ electrodes, FE-SEM images and absorption and action spectra of FTO/SnO_2/$(C_{60})_m$ electrodes (S6), and transient absorption spectra (S7), AFM images (S8), and XRD patterns (S9) of FTO/SnO_2/$(C_{70})_m$ electrodes. This material is available free of charge via the Internet at http://pubs.acs.org.

References and Notes

(1) (a) Whitesides, G. M.; Mathias, J. P.; Seto, C. T. *Science* **1991**, *254*, 1312. (b) Zhang, S. *Nat. Biotechnol.* **2003**, *21*, 1171. (c) Ariga, K.; Nakanishi, T.; Hill, J. P. *Curr. Opin. Colloid Interface Sci.* **2007**, *12*, 106. (d) Ariga, K.; Hill, J. P.; Lee, M. V.; Vinu, A.; Charvet, R.; Acharya, S. *Sci. Technol. Adv. Mater.* **2008**, *9*, 014109. (e) Mann, S. *Nat. Mater.* **2009**, *8*, 781.

(2) (a) Hasobe, T.; Imahori, H.; Kamat, P. V.; Fukuzumi, S. *J. Am. Chem. Soc.* **2003**, *125*, 14962. (b) Hill, J. P.; Jin, W.; Kosaka, A.; Fukushima, T.; Ichihara, H.; Shimomura, T.; Ito, K.; Hashizume, T.; Ishi, N.; Aida, T. *Science* **2004**, *304*, 1481. (c) Kovtyukhova, N. I.; Mallouk, T. E. *Adv. Mater.* **2005**, *17*, 187. (d) Yamamoto, Y.; Fukushima, T.; Suna, Y.; Ishii, N.; Saeki, A.; Seki, S.; Tagawa, S.; Taniguchi, M.; Kawai, T.; Aida, T. *Science* **2006**, *314*, 1761. (e) Imahori, H. *J. Mater. Chem.* **2007**, *17*, 31. (f) Imahori, H.; Umeyama, T. *J. Phys. Chem. C* **2009**, *113*, 9029.

(3) (a) Cassell, A. M.; Asplund, C. L.; Tour, J. M. *Angew. Chem., Int. Ed.* **1999**, *38*, 2403. (b) Brough, P.; Bonifazi, D.; Prato, M. *Tetrahedron* **2006**, *62*, 2110. (c) Wang, L.; Liu, B.; Liu, D.; Yao, M.; Hou, Y.; Yu, S.; Cui, T.; Li, D.; Zou, G.; Iwasiewicz, A.; Sundqvist, B. *Adv. Mater.* **2006**, *18*, 1883. (d) Tan, Z.; Masuhara, A.; Kasai, H.; Nakanishi, H.; Oikawa, H. *Jpn. J. Appl. Phys.* **2008**, *47*, 1426.

(4) (a) Jin, Y.; Curry, R. J.; Sloan, J.; Hatton, R. A.; Chong, L. C.; Blanchard, N.; Stolojan, V.; Kroto, H. W.; Silva, S. R. P. *J. Mater. Chem.* **2006**, *16*, 3715. (b) Ji, H.-X.; Hu, J.-S.; Tang, Q.-X.; Song, W.-G.; Wang, C.-R.; Hu, W.-P.; Wan, Li.-J.; Lee, S.-T. *J. Phys. Chem. C* **2007**, *111*, 10498. (c) Ji, H.-X.; Hu, J.-S.; Wan, Li.-J.; Tang, Q.-X.; Hu, W.-P. *J. Mater. Chem.* **2008**, *18*, 328. (d) Chong, L. C.; Sloan, J.; Wagner, G.; Silva, S. R. P.; Curry, R. J. *J. Mater. Chem.* **2008**, *18*, 3319.

(5) (a) Murakami, H.; Shirakusa, M.; Sagara, T.; Nakashima, N. *Chem. Lett.* **1999**, 815. (b) Guo, Y.-G.; Li, C.-J.; Wan, L.-J.; Chen, D.-M.; Wang, C.-R.; Bai, C.-L.; Wang, Y.-G. *Adv. Funct. Mater.* **2003**, *13*, 626. (c) Li, C.-J.; Guo, Y.-G.; Li, B.-S.; Wang, C.-R.; Wan, L.-J.; Bai, C.-L. *Adv. Mater.* **2005**, *17*, 71. (d) Geng, J.; Zhou, W.; Skelton, P.; Yue, W.; Kinloch, I. A.; Windle, A. H.; Johnson, B. F. G. *J. Am. Chem. Soc.* **2008**, *130*, 2527.

(6) (a) Miyazawa, K.; Kuwasaki, Y.; Obayashi, A.; Kuwabara, M. *J. Mater. Res.* **2002**, *17*, 83. (b) Miyazawa, K. *J. Am. Ceram. Soc.* **2002**, *85*, 1297. (c) Miyazawa, K.; Hamamoto, K.; Nagata, S.; Suga, T. *J. Mater. Res.* **2003**, *18*, 1096. (d) Sathish, M.; Miyazawa, K.; Sasaki, T. *Chem. Mater.* **2007**, *19*, 2398.

(7) (a) Georgakilas, V.; Pellarini, F.; Prato, M.; Guldi, D. M.; Melle-Franco, M.; Zerbetto, F. *Proc. Natl. Acad. Sci. U.S.A.* **2002**, *99*, 5075. (b) Liu, H.; Li, Y.; Jiang, L.; Luo, H.; Xiao, S.; Fang, H.; Li, H.; Zhu, D.; Yu, D.; Xu, J.; Xiang, B. *J. Am. Chem. Soc.* **2002**, *124*, 13370. (c) Miyazawa, K.; Minato, J.; Yoshii, T.; Fujino, M.; Suga, T. *J. Mater. Res.* **2005**, *20*, 688. (d) Guldi, D. M.; Gouloumis, A.; Vázquez, P.; Torres, T.; Georgakilas, V.; Prato, M. *J. Am. Chem. Soc.* **2005**, *127*, 5811. (e) Cha, S. I.; Miyazawa, K.; Kim, J.-D. *Chem. Mater.* **2008**, *20*, 1667.

(8) (a) Wang, L.; Li, B.; Liu, D.; Yao, M.; Yu, S.; Hou, Y.; Zou, B.; Cui, T.; Zou, G.; Sundqvist, B.; Luo, Z.; Li, H.; Li, Y.; Liu, J.; Chen, S.; Wang, G.; Liu, Y. *Appl. Phys. Lett.* **2007**, *91*, 103112. (b) Sathish, M.; Miyazawa, K. *J. Am. Chem. Soc.* **2007**, *129*, 13816. (c) Sathish, M.; Miyazawa, K.; Hill, J. P.; Ariga, K. *J. Am. Chem. Soc.* **2009**, *131*, 6372. (d) Wakahara, T.; Sathish, M.; Miyazawa, K.; Hu, C.; Tateyama, Y.; Nemoto, Y.; Sasaki, T.; Ito, O. *J. Am. Chem. Soc.* **2009**, *131*, 9940.

(9) (a) Nakanishi, T.; Ariga, K.; Michinobu, T.; Yoshida, K.; Takahashi, H.; Teranishi, T.; Möhwald, H.; Kurth, D. G. *Small* **2007**, *3*, 2019. (b) Nakanishi, T.; Michinobu, T.; Yoshida, K.; Shirahata, N.; Ariga, K.; Möhwald, H.; Kurth, D. G. *Adv. Mater.* **2008**, *20*, 443.

(10) (a) Bokare, A. D.; Patnaik, A. *J. Phys. Chem. B* **2003**, *107*, 6079. (b) Fujita, N.; Yamashita, T.; Asai, M.; Shinkai, S. *Angew. Chem., Int. Ed.* **2005**, *44*, 1257. (c) Deguchi, S.; Mukai, S. *Chem. Lett.* **2006**, *35*, 396. (d) Kawauchi, T.; Kumaki, J.; Yashima, E. *J. Am. Chem. Soc.* **2006**, *128*, 10560. (e) Li, B.; Tao, X.; Kasai, H.; Oikawa, H.; Nakanishi, H. *Mater. Lett.* **2007**, *61*, 1738.

(11) (a) Brettreich, M.; Burghardt, S.; Böttcher, C.; Bayerl, T.; Bayerl, S.; Hirsh, A. *Angew. Chem., Int. Ed.* **2000**, *39*, 1845. (b) Zhou, S.; Burger, C.; Chu, B.; Sawamura, M.; Nagahama, N.; Toganoh, M.; Hackler, U. E.; Isobe, H.; Nakamura, E. *Science* **2001**, *291*, 1944. (c) Sawamura, M.; Kawai, K.; Matsuo, Y.; Kanie, K.; Kato, T.; Nakamura, E. *Nature* **2002**, *419*, 702. (d) Hotta, H.; Kang, S.; Umeyama, T.; Matano, Y.; Yoshida, K.; Isoda, S.; Imahori, H. *J. Phys. Chem. B* **2005**, *109*, 5700. (e) Nakanishi, T.; Schmitt, W.; Michinobu, T.; Kurth, D. G.; Ariga, K. *Chem. Commun.* **2005**, 5982. (f) Masuhara, A.; Tan, Z.; Kasai, H.; Nakanishi, H.; Oikawa, H. *Jpn. J. Appl. Phys.* **2009**, *48*, 050206.

(12) (a) Hoppe, H.; Sariciftci, N. S. *J. Mater. Chem.* **2006**, *16*, 45. (b) Yang, X.; Loos, J. *Macromolecules* **2007**, *40*, 1353. (c) Günes, S.; Neugebauer, H.; Sariciftci, N. S. *Chem. Rev.* **2007**, *107*, 1324. (d) Thompson, B. C.; Fréchet, J. M. J. *Angew. Chem., Int. Ed.* **2008**, *47*, 58.

(13) (a) Hoppe, H.; Niggemann, M.; Winder, C.; Kraut, J.; Hiesgen, R.; Hinsch, A.; Meissner, D.; Sariciftci, N. S. *Adv. Funct. Mater.* **2004**, *14*, 1005. (b) Yang, X.; van Duren, J. K. J.; Janssen, R. A. J.; Michels, M. A. J.; Loos, J. *Macromolecules* **2004**, *37*, 2151. (c) Yang, X.; Loos, J.; Veenstra, S. C.; Verhees, W. J. H.; Wienk, M. M.; Kroon, J. M.; Michels, M. A. J.; Janssen, R. A. J. *Nano. Lett.* **2005**, *5*, 579. (d) Swinnen, A.; Haeldermans, I.; vande Ven, M.; D'Haen, J.; Vanhoyland, G.; Aresu, S.; D'Olieslaeger, M.; Manca, J. *Adv. Funct. Mater.* **2006**, *16*, 760. (e) Peet, J.; Kim, J. Y.; Coates, N. E.; Ma, W. L.; Moses, D.; Heeger, A. J.; Bazan, G. C. *Nat. Mater.* **2007**, *6*, 497. (f) Lee, J. K.; Ma, W. L.; Brabec, C. J.; Yuen, J.; Moon, J. S.; Kim, J. Y.; Lee, K.; Bazan, G. C.; Heeger, A. J. *J. Am. Chem. Soc.* **2008**, *130*, 3619.

(14) (a) Xing, Y. J.; Jing, G. Y.; Xu, J.; Yu, D. P.; Liu, H. B.; Li, Y. L. *Appl. Phys. Lett.* **2005**, *87*, 263117. (b) Somani, P. R.; Somani, S. P.; Umeno, M. *Appl. Phys. Lett.* **2007**, *91*, 173503. (c) Shin, H. S.; Yoon, S. M.; Tang, Q.; Chon, B.; Joo, T.; Choi, H. C. *Angew. Chem., Int. Ed.* **2008**, *47*, 693. (d) Lu, G.; Li, L.; Yang, X. *Small* **2008**, *4*, 601. (e) Bai, R.; Ouyang, M.; Li, Z.-Z.; Yang, L.-G.; Shi, M.-M.; Wu, G.; Wang, M.; Chen, H.-Z. *J. Mater. Chem.* **2008**, *18*, 4318. (f) Hasobe, T.; Sandanayaka, A. S. D.; Wada, T.; Araki, Y. *Chem. Commun.* **2008**, 3372.

(15) (a) Hasobe, T.; Imahori, H.; Kamat, P. V.; Ahn, T. K.; Kim, S. K.; Kim, D.; Fujimoto, A.; Hirakawa, T.; Fukuzumi, S. *J. Am. Chem. Soc.* **2005**, *127*, 1216. (b) Hosomizu, K.; Imahori, H.; Hahn, U.; Nierengarten, J.-F.; Listorti, A.; Armaroli, N.; Nemoto, T.; Isoda, S. *J. Phys. Chem. C* **2007**, *111*, 2777. (c) Umeyama, T.; Tezuka, N.; Fujita, M.; Hayashi, S.; Kadota, N.; Matano, Y.; Imahori, H. *Chem.—Eur. J.* **2008**, *14*, 4875.

(16) (a) Sun, Y.-P.; Bunker, C. E. *Nature* **1993**, *365*, 398. (b) Sun, Y.-P.; Bunker, C. E. *Chem. Mater.* **1994**, *6*, 578. (c) Sun, Y.-P.; Ma, B.; Bunker, C. E.; Liu, B. *J. Am. Chem. Soc.* **1995**, *117*, 12705.

(17) (a) Ghosh, H. N.; Sapre, A. V.; Mittal, J. P. *J. Phys. Chem.* **1996**, *100*, 9439. (b) Fujitsuka, M.; Kasai, H.; Masuhara, A.; Okada, S.; Oikawa,

H.; Nakanishi, H.; Watanabe, A.; Ito, O. *Chem. Lett.* **1997**, 1211. (c) Thomas, K. G.; Biju, V.; Guldi, D. M.; Kamat, P. V.; George, M. V. *J. Phys. Chem. B* **1999**, *103*, 8864. (d) Nath, S.; Pal, H.; Sapre, A. V. *Chem. Phys. Lett.* **2000**, *327*, 143. (e) Alargova, R. G.; Deguchi, S.; Tsujii, K. *J. Am. Chem. Soc.* **2001**, *123*, 10460. (f) Saha, A.; Mukherjee, A. K. *J. Chem. Phys.* **2005**, *122*, 184504. (g) Datta, K.; Mukherjee, A. K. *J. Chem. Phys.* **2006**, *124*, 144509.

(18) (a) Kamat, P. V.; Barazzouk, S.; Thomas, K. G.; Hotchandani, S. *J. Phys. Chem. B* **2000**, *104*, 4014. (b) Kamat, P. V.; Barazzouk, S.; Hotchandani, S.; Thomas, K. G. *Chem.—Eur. J.* **2000**, *6*, 3914. (c) Barazzouk, S.; Hotchandani, S.; Kamat, P. V. *Adv. Mater.* **2001**, *13*, 1614. (d) Kutner, W.; Pieta, P.; Nowakowski, R.; Sobczak, J. W.; Kaszkur, Z.; McCarty, A. L.; D'Souza, F. *Chem. Mater.* **2005**, *17*, 5635.

(19) (a) Nath, S.; Pal, H.; Sapre, A. V. *Chem. Phys. Lett.* **2002**, *360*, 422. (b) Nath, S.; Pal, H.; Sapre, A. V. *Chem. Phys. Lett.* **2003**, *369*, 394.

(20) (a) Umeyama, T.; Tezuka, N.; Seki, S.; Matano, Y.; Nishi, M.; Hirao, K.; Lehtivuori, H.; Tkachenko, N. V.; Lemmetyinen, H.; Nakao, Y.; Sakaki, S.; Imahori, H. *Adv. Mater.* DOI: 10.1002/adma.200903056. (b) Tezuka, N.; Umeyama, T.; Seki, S.; Matano, Y.; Nishi, M.; Hirao, K.; Imahori, H. *J. Phys. Chem. C* DOI: 10.1021/jp910832a.

(21) Sivaraman, N.; Dhamodaran, R.; Kaliappan, I.; Srinivasan, T. G.; Vasudeva Rao, P. R.; Mathews, C. K. *Fullerene Sci. Technol.* **1994**, *2*, 233.

(22) (a) Grozema, F. C.; Siebbeles, L. D. A.; Warman, J. M.; Seki, S.; Tagawa, S.; Scherf, U. *Adv. Mater.* **2002**, *14*, 228. (b) Saeki, A.; Seki, S.; Koizumi, Y.; Sunagawa, T.; Ushida, K.; Tagawa, S. *J. Phys. Chem. B* **2005**, *109*, 10015. (c) Amaya, T.; Seki, S.; Moriuchi, T.; Nakamoto, K.; Nakata, T.; Sakane, H.; Saeki, A.; Tagawa, S.; Hirao, T. *J. Am. Chem. Soc.* **2009**, *131*, 408.

(23) Tkachenko, N. V.; Rantala, L.; Tauber, A. Y.; Helaja, J.; Hynninen, P. H.; Lemmetyinen, H. *J. Am. Chem. Soc.* **1999**, *121*, 9378.

(24) We examined the effects of volume ratio of good solvent-acetonitrile on the incident photon-to-current efficiency (IPCE) value. The volume ratio (1:4) was found to be an optimized condition with respect to the IPCE value.

(25) Ajie, H.; Alvarez, M. M.; Anz, S. J.; Beck, R. D.; Diederich, F.; Fostiropoulos, K.; Huffman, D. R.; Krätschmer, W.; Rubin, Y.; Schriver, K. E.; Sensharma, D.; Whetten, R. L. *J. Phys. Chem.* **1990**, *94*, 8630.

(26) The ratio of rodlike and particulate clusters is estimated to be ~1:2 by counting the numbers of the clusters in the FE-SEM image of the deposited film (Figure 4c).

(27) In case of the electrode deposited from ANS-AN mixture, absorbance at 400 nm is relatively low (0.61) compared to the films prepared from the other solvent mixtures, because some parts of the deposited film inevitably exfoliate when pulled up from the cluster solution after completion of the electrophoretic process. However, the photocurrent generation efficiency based on the number of absorbed photons is calculated to be 3.3%, which is smaller than the IPCE value of the electrode prepared from BZN-AN (4.5%). Hence, given the high light-harvesting efficiency at 400 nm in the other deposited films, the light-harvesting efficiency is not a major factor determining the photocurrent generation in the present systems.

(28) The film morphologies, absorption spectra, and photocurrent action spectra of $(C_{60})_m$-modified electrodes, prepared from BZ-AN, CB-AN, and ANS-AN mixtures, are summarized in Supporting Information Figure S6, which have not been reported in the previous studies.[15,18]

(29) (a) Arbogast, J. W.; Foote, C. S. *J. Am. Chem. Soc.* **1991**, *113*, 8886. (b) Wasielewski, M. R.; O'Neil, M. P.; Lykke, K. R.; Pellin, M. J.; Gruen, D. M. *J. Am. Chem. Soc.* **1991**, *113*, 2774.

(30) Allemand, P.-M.; Koch, A.; Wudl, F.; Rubin, Y.; Diederich, F.; Alvarez, M. M.; Anz, S. J.; Whetten, R. L. *J. Am. Chem. Soc.* **1991**, *113*, 1050.

(31) To shed light on the excited state dynamics, we performed the subpicosecond to nanosecond time-resolved transient absorption measurements on the FTO/SnO_2/$(C_{70})_m$ electrodes prepared from BZ-AN and CB-AN (Supporting Information Figure S7). Both of them show ground-state bleaching around 550 nm and excited state absorption at > 650 nm. Although the maximum IPCE values are significantly different (4.6 and 0.8%, respectively), there seemed to be no considerable difference in the excited state lifetimes of C_{70}. Therefore, the excited state lifetimes of C_{70} do not affect the difference in the IPCE values.

(32) X-ray photoelectron spectroscopy measurements on the deposited film samples did not reveal any peaks originating from remaining solvents (e.g., Cl, in the case of the sample prepared from DCB-AN mixture). Therefore, we can rule out any possible effects of residual solvents on electron mobility.

(33) (a) Kang, S.; Umeyama, T.; Ueda, M.; Matano, Y.; Hotta, H.; Yoshida, K.; Isoda, S.; Shiro, M.; Imahori, H. *Adv. Mater.* **2006**, *18*, 2549. (b) Imahori, H.; Ueda, M.; Kang, S.; Hayashi, H.; Hayashi, S.; Kaji, H.; Seki, S.; Saeki, A.; Tagawa, S.; Umeyama, T.; Matano, Y.; Yoshida, K.; Isoda, S.; Shiro, M.; Tkachenko, N. V.; Lemmetyinen, H. *Chem.—Eur. J.* **2007**, *13*, 10182.

(34) Vaughan, G. B. M.; Heiney, P. A.; Fischer, J. E.; Luzzi, D. E.; Ricketts-Foot, D. A.; McGhie, A. R.; Hui, Y.-W.; Smith, A. L.; Cox, D. E.; Romanow, W. J.; Allen, B. H.; Coustel, N.; McCauley, J. P., Jr.; Smith, A. B., III *Science* **1991**, *254*, 1350.

(35) Time-of-flight (TOF) technique is suitable to evaluate the electron mobility of the entire films with the thickness of more than several hundreds of nanometer. However, intense surface roughness of the deposited films did not allow us to apply TOF method to the electrophoretically deposited $(C_{70})_m$ films.

(36) (a) Martin, T. P.; Näher, U.; Schaber, H.; Zimmermann, U. *Phys. Rev. Lett.* **1993**, *70*, 3079. (b) Branz, W.; Malinowski, N.; Schaber, H.; Martin, T. P. *Chem. Phys. Lett.* **2000**, *328*, 245. (c) Branz, W.; Malinowski, N.; Enders, A.; Martin, T. P. *Phys. Rev. B* **2002**, *66*, 094107.

JP911141S